Supplement of Earth Syst. Sci. Data, 10, 2069–2095, 2018
https://doi.org/10.5194/essd-10-2069-2018-supplement

Open Access Earth System Science Data

Supplement of

The Berkeley High Resolution Tropospheric NO_2 product

J. L. Laughner et al.

Correspondence to: Ronald C. Cohen (rccohen@berkeley.edu)

S1 New visible-only AMF formulation introduced in v3.0A

As described in the methods (Sect. 2.1), BEHR has, since v2.1C, included both a total tropospheric NO_2 column and a "visible-only" column. Figure S1 provides a graphic definition of these terms. The visible-only column includes the NO_2 that would be visible if observing the pixel from directly above: for the cloudless part of the pixel, the column extends to the ground, but for the cloud covered part it only extends down to the cloud top. In contrast the standard total tropospheric column is the sum of the visible-only column and the ghost column, where the ghost column is the NO_2 below the clouds.

The AMF necessary to convert the observed slant columns to a visible-only vertical column (a what we will term a "visible-only" AMF) can be conceptualized two different ways. The formula for the v3.0 visible-only AMF is given in Eq. (3). Conceptually, this is the model SCD divided by the modeled VCD. In v2.1C, an alternate formulation was used:

$$A_{\mathrm{BEHR,vis}} = (1 - f)A_{\mathrm{clear,vis}} + fA_{\mathrm{cloudy,vis}} \tag{S1}$$

where f is again the cloud radiance fraction and

$$A_{\mathrm{clear,vis}} = \frac{\int_{p_{\mathrm{surf}}}^{p_{\mathrm{trop}}} w_{\mathrm{clear}}(p)g(p)\,dp}{\int_{p_{\mathrm{surf}}}^{p_{\mathrm{trop}}} g(p)\,dp} \tag{S2}$$

$$A_{\mathrm{cloudy,vis}} = \frac{\int_{p_{\mathrm{cloud}}}^{p_{\mathrm{trop}}} w_{\mathrm{cloudy}}(p)g(p)\,dp}{\int_{p_{\mathrm{cloud}}}^{p_{\mathrm{trop}}} g(p)\,dp} \tag{S3}$$

This earlier method assumes that each pixel can be treated as two totally independent subpixels, one clear and one cloudy. This seems a logical extension of the independent pixel

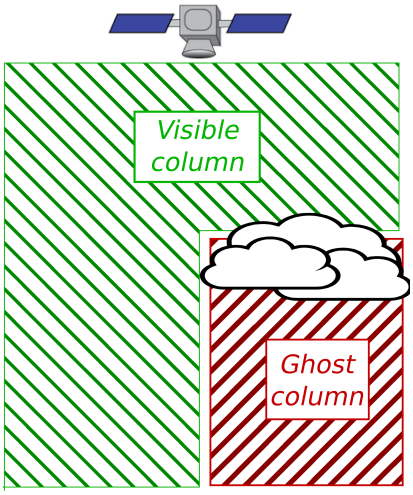

Figure S1: A graphical example of the definitions of visible and ghost columns.

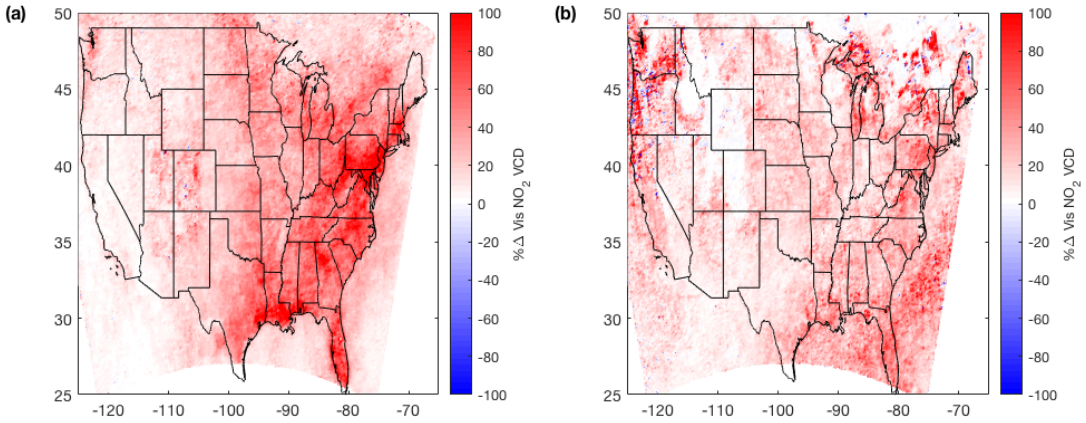

Figure S2: The change in the BEHR visible-only NO_2 VCDs resulting from the new AMF formulation, averaged for **(a)** JJA and **(b)** DJF, 2012. The NO_2 columns are calculated using the new NASA SCDs, BRF land surface reflectance, and the new ocean surface reflectance LUT.

approximation (Cahalan et al., 1994; Marshak et al., 1998), but the physical interpretation is less clear than the new formulation.

Although both approaches to calculating a visible-only AMF (i.e. Eq. S1 and Eq. 3) are conceptually valid , they are not mathematically identical, and so the retrieved visible tropospheric NO_2 column increases between v2.1C and v3.0A Figure S2 shows the average change in visible-only NO_2 columns when changing from the v2.1C AMF to the v3.0A AMF. In the summer (Fig. S2a) the average increase approaches 100% over the eastern US, decreasing to 0 towards the west coast. In the winter (Fig. S2b) the difference is more sporadic.

The main cause for the change is the difference in how the relative magnitude of the NO_2 to-ground VCD and the above-cloud VCD is treated by the AMF calculation. In the v2.1C visible-only AMF formulation, the relative contribution of the clear- and cloudy- sky AMFs was entirely determined by the cloud radiance fraction. Equation (S1) can be written as:

$$A_{\mathrm{BEHR,vis}} = (1-f)\frac{S_{\mathrm{clear}}}{V_{\mathrm{clear}}} + f\frac{S_{\mathrm{cloudy}}}{V_{\mathrm{cloudy}}} \tag{S4}$$

where f is the cloud radiance fraction, S_{clear} and V_{clear} are the modeled slant and vertical NO_2 column density for the clear part of the pixel and S_{cloudy} and V_{cloudy} are likewise the modeled slant and vertical column density for the cloudy part of the pixel. V_{clear} and V_{cloudy} may be very different magnitudes (by a factor of up to 1000), especially in polluted areas where most of the NO_2 is near the surface and therefore below the cloud. However, the slant columns are related to their corresponding vertical columns through the scattering weights, which typically means the corresponding S and V values will be within about a factor of 2 or 3 of each other. This means that, in Eq. (S4), the relative magnitudes of $S_{\mathrm{clear}}/V_{\mathrm{clear}}$ versus $S_{\mathrm{cloudy}}/V_{\mathrm{cloudy}}$ will be similar, even if V_{clear} and V_{cloudy} (and likewise S_{clear} and S_{cloudy}) are substantially different.

In contrast, the new formulation could be written as:

$$A_{\mathrm{BEHR,vis,new}} = \frac{(1-f)S_{\mathrm{clear}} + fS_{\mathrm{cloudy}}}{(1-f_g)V_{\mathrm{clear}} + f_g V_{\mathrm{cloudy}}} \tag{S5}$$

where f_g is the geometric cloud fraction. In this case, the relative magnitudes of S_{clear} versus S_{cloudy} and V_{clear} versus V_{cloudy} does matter. If $V_{\mathrm{cloudy}} \ll V_{\mathrm{clear}}$ (which implies $S_{\mathrm{cloudy}} \ll S_{\mathrm{clear}}$), then Eq. S5 reduces to

$$A_{\mathrm{BEHR,vis,new}} = \frac{(1-f)S_{\mathrm{clear}}}{(1-f_g)V_{\mathrm{clear}}} \tag{S6}$$

whereas in Eq. (S4), the second term does not go to zero when $V_{\mathrm{cloudy}} \ll V_{\mathrm{clear}}$ because $S_{\mathrm{cloudy}} \propto V_{\mathrm{cloudy}}$. This means that, in theory, when $V_{\mathrm{cloudy}} \ll V_{\mathrm{clear}}$, the new visible-only

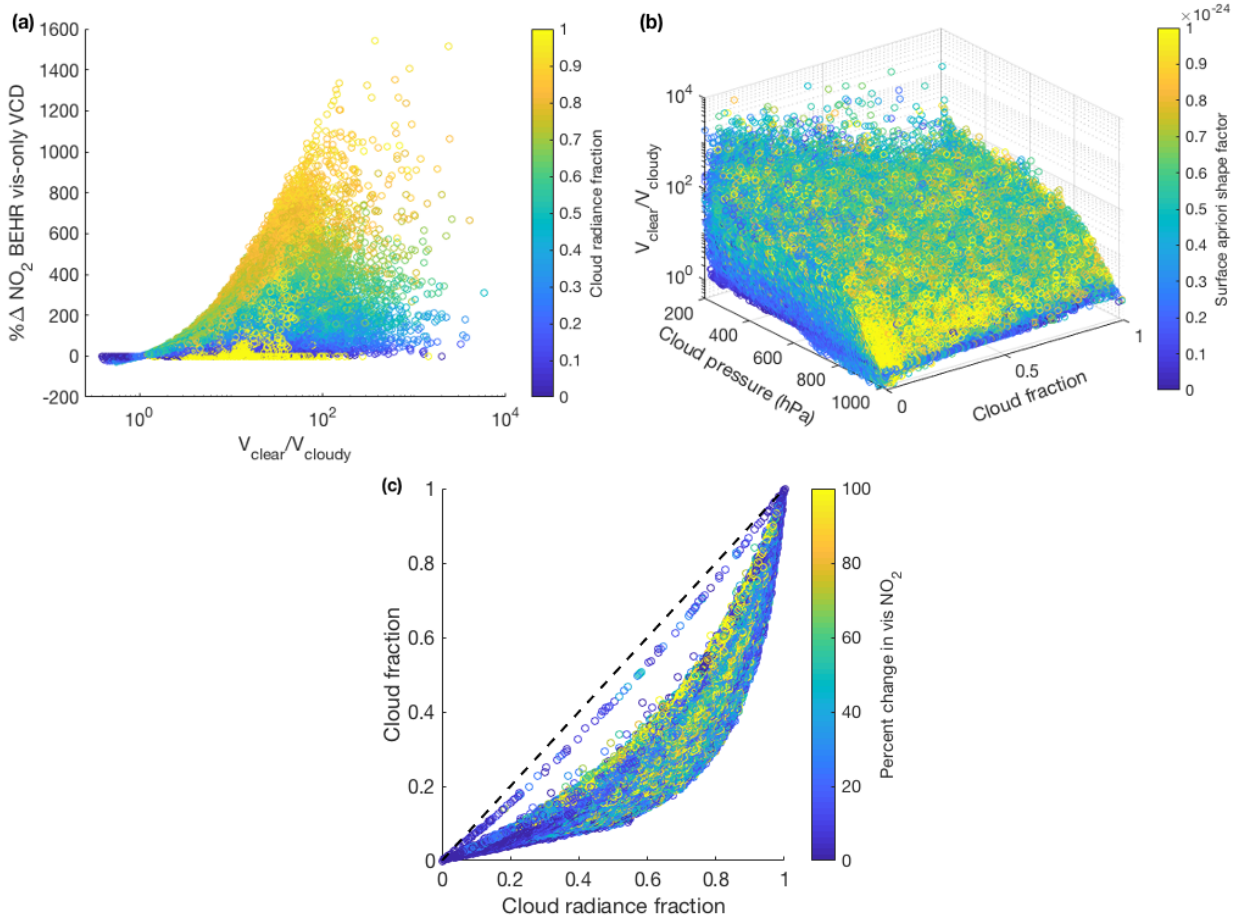

Figure S3: **(a)** The percent change in the visible-only BEHR NO_2 VCD versus the ratio modeled VCDs (V_{clear}, the WRF-Chem profiles integrated over the whole troposphere) to those integrated from cloud top to tropopause (V_{cloudy}), colored by cloud radiance fraction. **(b)** The ratio of $V_{\text{clear}}/V_{\text{cloudy}}$ versus geometric cloud fraction, cloud pressure, and colored by shape factor (mixing ratio/V_{clear}) at the surface. **(c)** The percent change in visible-only NO_2 VCD as a function of cloud radiance fraction and geometric cloud fraction. The black dashed line in (c) is the 1:1 line. *Note:* the color scale saturates at 10^{-24} in (b) and 100% in (c) to emphasize the distribution of the percent changes.

AMF will essentially be a clear sky AMF, which will be less than a cloudy sky AMF since it includes near-surface NO_2 that OMI is less sensitive to. In contrast, in the old formulation, the relative contribution of the clear and cloudy components only depends on the cloud radiance fraction, not the relative magnitude of V_{clear} and V_{cloudy}, so the old visible-only AMFs will more often be of similar magnitude to a cloudy AMF. Because $V = S/A$ and $A_{\text{clear}} < A_{\text{cloudy}}$ in most cases, this means that the new visible-only NO_2 columns will be much larger than the old one.

In Fig. S3, we examine whether these effects show up in the BEHR data. Figure S3a shows the relative change in the visible-only NO_2 columns versus the ratio of $V_{\text{clear}}/V_{\text{cloudy}}$. The ratio $V_{\text{clear}}/V_{\text{cloudy}}$ sets a clear upper bound on the difference between the old and new visible-only NO_2 VCDs. What controls the ratio $V_{\text{clear}}/V_{\text{cloudy}}$ is shown in Fig. S3b. It increases rapidly as cloud pressure decreases, i.e. as the cloud hides more of the surface NO_2. When a large fraction of the NO_2 is near the surface, the effect is larger. This is illustrated by the fact that the top of the scatter in Fig. S3b has the greater surface NO_2 shape factor (here, the NO_2 mixing ratio divided by the column density). For a given cloud pressure, increasing the cloud fraction also increases $V_{\text{clear}}/V_{\text{cloudy}}$. All of these relationships are a natural result of clouds covering more NO_2.

In Fig. S3a, we also see that for a given ratio $V_{\text{clear}}/V_{\text{cloudy}}$, the magnitude of the difference between old and new BEHR NO_2 VCDs can vary quite significantly, depending primarily on the cloud radiance fraction. As the cloud radiance fraction decreases, the second term in both Eq. (S4) and Eq. (S5) becomes less important, so both become more similar to a clear-sky AMF and each other. However, at cloud radiance fractions near 1, the difference between old and new BEHR VCDs drops to 0. This happens because, as shown in Fig. S3c, when the cloud fractions are near 0 or 1, the geometric and radiance fractions converge, and for $f_g = f = 0$ or $f_g = f = 1$, Eq. (S4) and (S5) reduce to the same quantities.

To summarize, the conceptual difference is that the old AMF was a weighted sum of the clear and cloudy AMFs, but this did not account for the difference in magnitude between the to-ground and above cloud columns. The new AMF is a ratio of the expected slant column to the expected visible vertical column, which tends to include more NO_2 from the clear part of the pixel. Since OMI is less sensitive overall to NO_2 in the clear part under most circumstances, the new AMFs are smaller, resulting in larger retrieved visible-only VCDs.

S2 Difference in average VCDs due to profile temporal resolution

In Sect. 4.3.2 of the main paper, we concluded that the statistically skewed distribution of NO_2 in the upper troposphere (UT) caused by lightning was the cause of the large difference between NO_2 VCDs in the SE US calculated with monthly or daily a priori profiles. We can see this is Fig. S5. In the SE, the average NO_2 profiles are the same whether we use

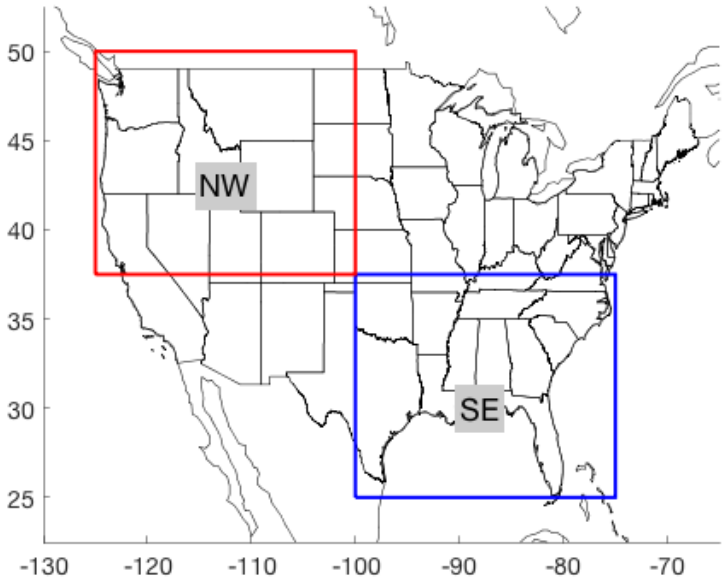

Figure S4: Regions used in testing the differences between using monthly and daily a priori NO_2 profiles.

monthly or daily profiles (as expected, since an average of averages should be equal to a single average over all the data, given proper weighting). However, the median profiles are very different. In the NW, where there is little lightning, both the mean and median of the daily and monthly profiles match.

To complement the qualitative discussion in the main paper, here, we will present a mathematical argument for why a different average shape factor can result from the average of already averaged monthly profiles versus averaging daily profiles. The difference in the NO_2 VCDs when using daily vs. monthly profiles must ultimately be due to differences in the AMFs. Consider an average AMF for a given location defined by:

$$\overline{A} = \frac{1}{n} \sum_{i=1}^{n} \frac{\int_{p_{s_i}}^{p_t} w_i(p) g_i(p)\, dp}{\int_{p_{s_i}}^{p_t} g_i(p)\, dp} \tag{S7}$$

For a given location, the surface pressure and (over the course of a month) surface reflectivity will be fairly constant, and additionally let us assume that the sun-satellite geometry will average in such a way that the scattering weights, w_i can be taken as an average, $\overline{w}$. With this assumption and assuming that $p_{s_i} = p_s$ for all i:

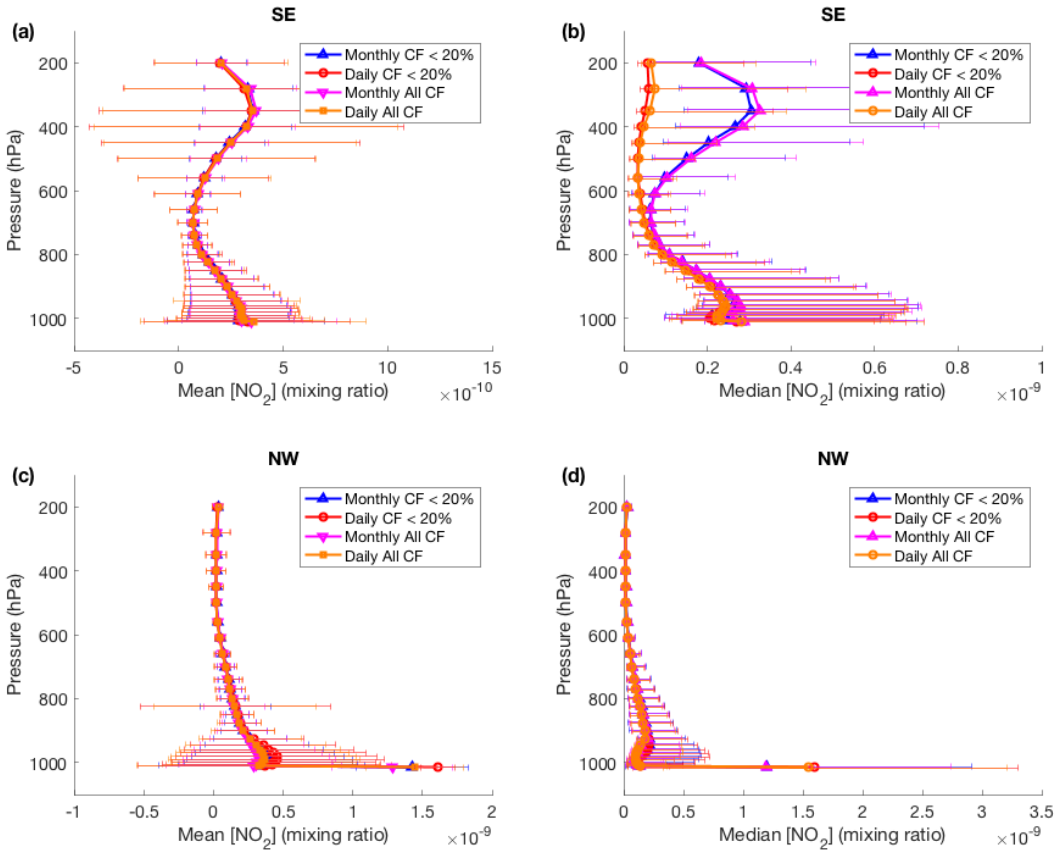

Figure S5: Mean (a,c) and median (b,d) NO_2 a priori profiles for the regions defined in S4 (southeast, a–b; northwest, c–d). Error bars for means are 1σ standard deviation, medians are the 25th and 75th percentiles. The blue and red lines only include pixels with cloud fraction $< 20\%$, while the magenta and orange lines include all pixels.

$$\overline{A} = \frac{1}{n}\sum_{i=1}^{n} \frac{\int_{p_s}^{p_t} \overline{w}(p) g_i(p)\, dp}{\int_{p_s}^{p_t} g_i(p)\, dp} \tag{S8}$$

$$= \int_{p_s}^{p_t} \overline{w}(p) \frac{1}{n}\sum_{i=1}^{n} S_i(p)\, dp \tag{S9}$$

where

$$S_i(p) = \frac{g_i(p)}{\int_{p_s}^{p_t} g_i(p)\, dp} \tag{S10}$$

i.e. $S_i(p)$ is the shape factor.

For the monthly average profiles, $g(p)$ is averaged temporally. Within each day, individual hours are weighted by their proximity to OMI overpass; the resulting daily average profiles are given equal weight in the monthly average:

$$\overline{g}(p) = \frac{1}{n}\sum_{i=1}^{n} g_i(p) \tag{S11}$$

where $g_i(p)$ represents one day's profile. Therefore, the monthly average shape factor is

$$\overline{S}_M(p) = \frac{1}{n}\sum_{i=1}^{n} \frac{\overline{g}(p)}{\int_{p_s}^{p_t} \overline{g}(p)\, dp} \tag{S12}$$

$$= \frac{\overline{g}(p)}{\int_{p_s}^{p_t} \overline{g}(p)\, dp} \tag{S13}$$

$$= \frac{\frac{1}{n}\sum_{i=1}^{n} g_i(p)}{\int_{p_s}^{p_t} \frac{1}{n}\sum_{i=1}^{n} g_i(p)\, dp} \tag{S14}$$

In contrast, the average shape factor using daily profiles would be:

$$\overline{S}_D(p) = \frac{1}{n}\sum_{i=1}^{n} \frac{g_i(p)}{\int_{p_s}^{p_t} g_i(p)\, dp} \tag{S15}$$

Eq. (S14) and (S15) are not mathematically equivalent. From Figs. S5 and 5, we can infer that the daily variation in surface NO_2 does not significantly affect the average AMF,

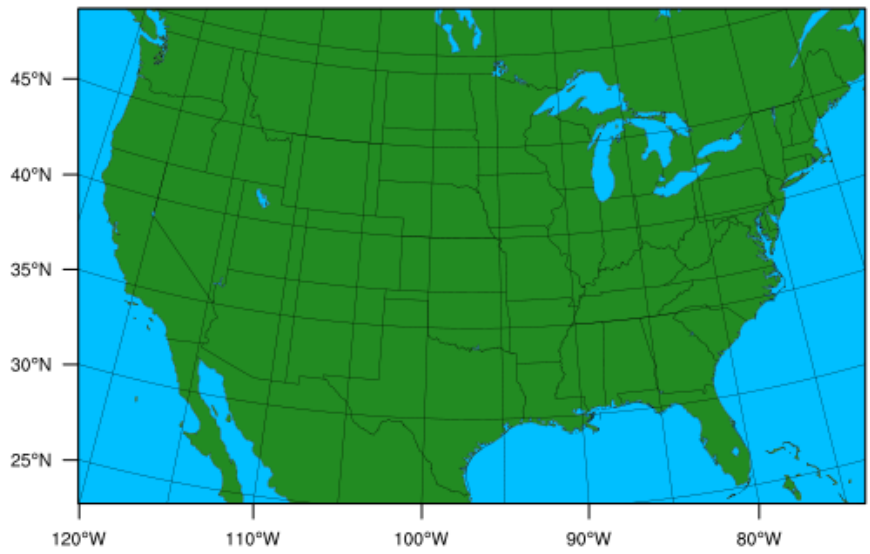

Figure S6: The WRF-Chem model domain.

which is consistent with Laughner et al. (2016), where implementing daily profiles led to small changes in the average over most of the domain. In Eq. (S15), profiles influenced by lightning will have a larger denominator than those not influenced, and so the increase in UT NO_2 is offset by the increase in total VCD. This causes the shift towards more surface influence in the average daily shape factors in Fig. 5c. Alternately, the denominator of Eq. (S15) can be viewed as a weighting factor that is inherently smaller for lightning-influenced profiles; thus, such profiles have less influence in the shape factor.

S3 WRF-Chem Model

For years 2005–2006, the chemical initial and boundary conditions for WRF-Chem are taken from the GEOS-Chem v9-02 model with the following changes to the chemistry:

- The rate of the reaction $NO_2 + OH \longrightarrow HNO_3$ is changed from that recommended in Sander et al. (2011) to that in Henderson et al. (2012).
- The rates of the formation and dissociation of HNO_4 are changed from that recommended in Sander et al. (2011) to that in Bacak et al. (2011).
- The rate of hydrolysis of N_2O_5 to HNO_3 was reduced to 10% of the value from Evans and Jacob (2005), as recommended in Brown et al. (2009).
- The number of moles of NO emitted per lightning flash was increased by 33% to 665 mol NO $flash^{-1}$ (midlatitudes) and 346 mol NO $flash^{-1}$ (tropics) based on the findings of Nault et al. (2017)

To provide output for WRF-Chem boundary conditions from 2005–2006, the GEOS-Chem model is spun up for the calendar year 2004.

S4 Additional figures

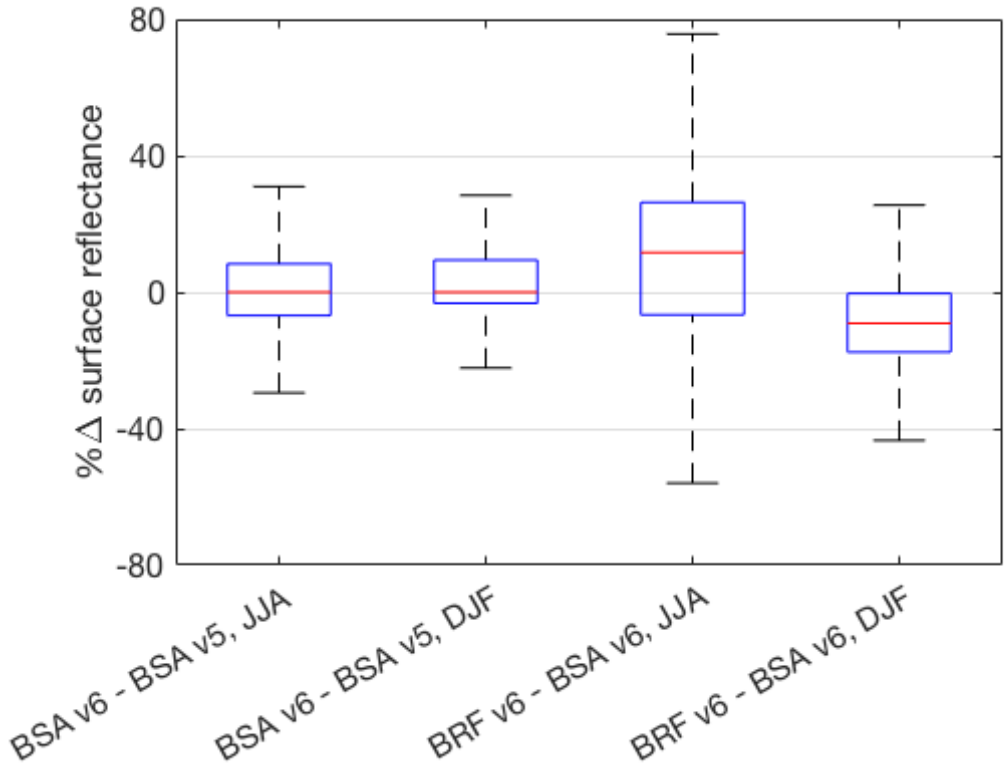

Figure S7: Box plots of percent difference in individual pixels' surface reflectances for pixels classified as land pixels, illustrating changes in individual pixels' surface reflectances are more variable changing from a black-sky to BRF surface reflectance than when just updating the version of the black-sky reflectance. The red line marks the median, the blue box the upper and lower quartiles, and the black lines the largest and smallest non-outlier values. Outliers are omitted.

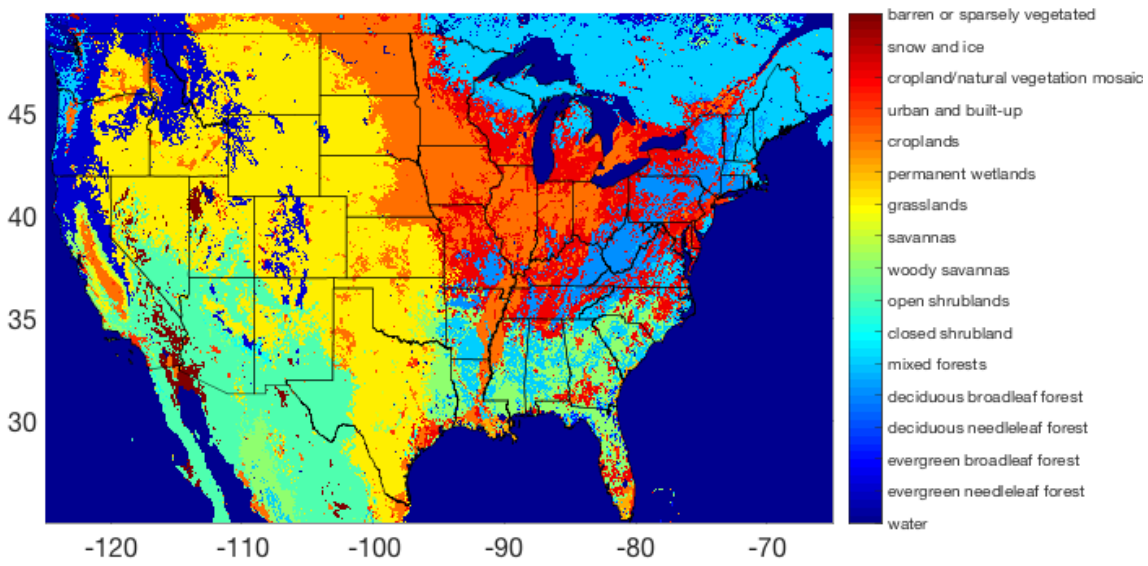

Figure S8: IGBP land cover classifications for 2012 from the MODIS MCD12C1 product

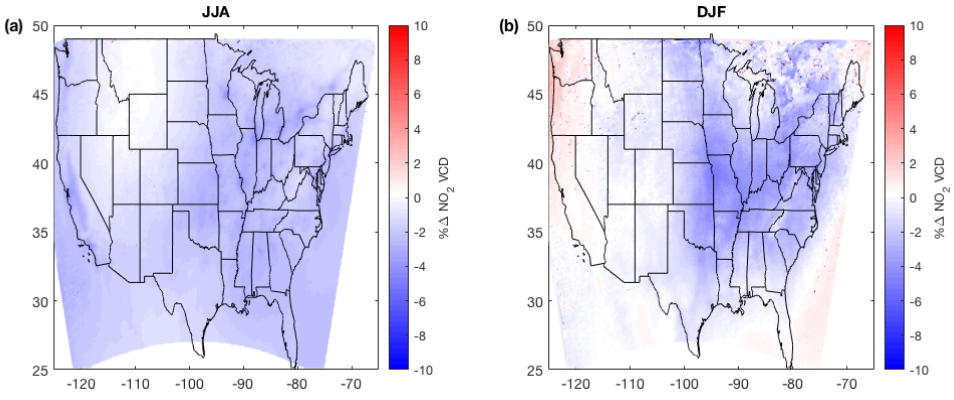

Figure S9: The percent change in total tropospheric VCDs after fixing the temperature lookup error (a) in summer (Jun–Aug) and (b) in winter (Jan, Feb, Dec).

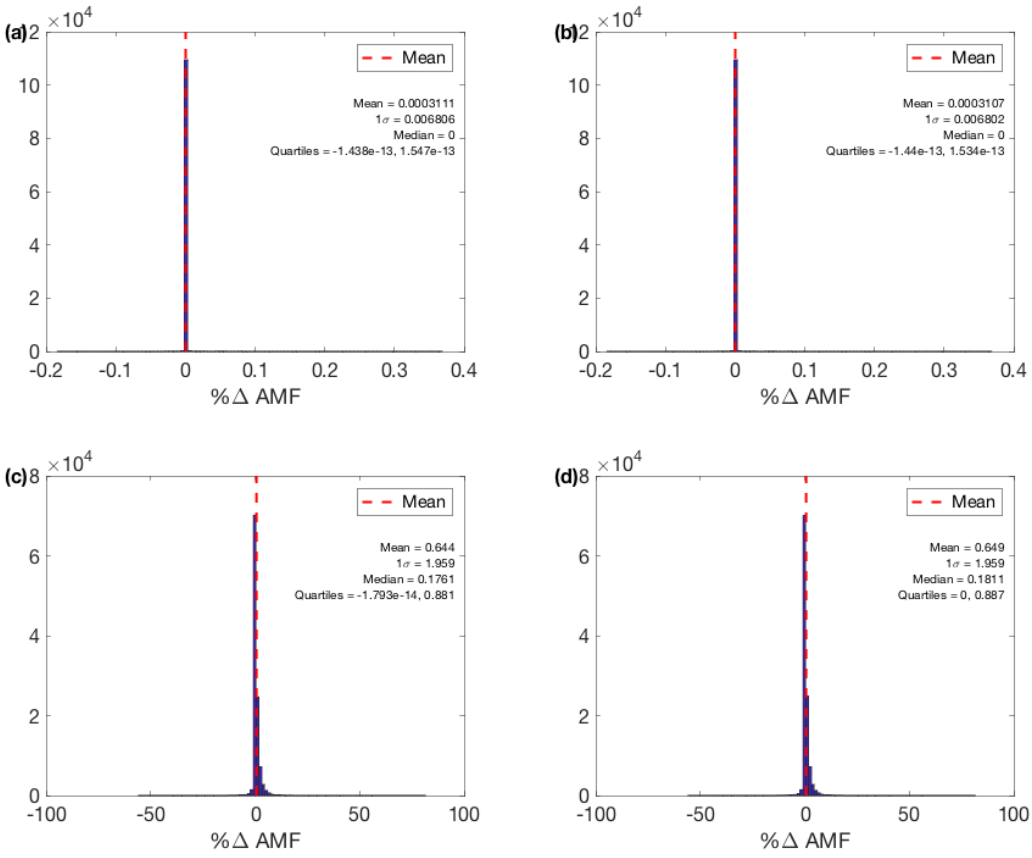

Figure S10: Percent differences between BEHR AMFs and AMFs recalculated with the published scattering weights and NO_2 a priori profiles. **(a, b)** use separate published clear and cloudy scattering weights, **(c, d)** use the v3.0A and previous cloud radiance fraction weighted average scattering weights. **(a)** and **(c)** are for total tropospheric AMFs, **(b)** and **(d)** are for visible-only AMFs.

S5 More detail on each incremental change

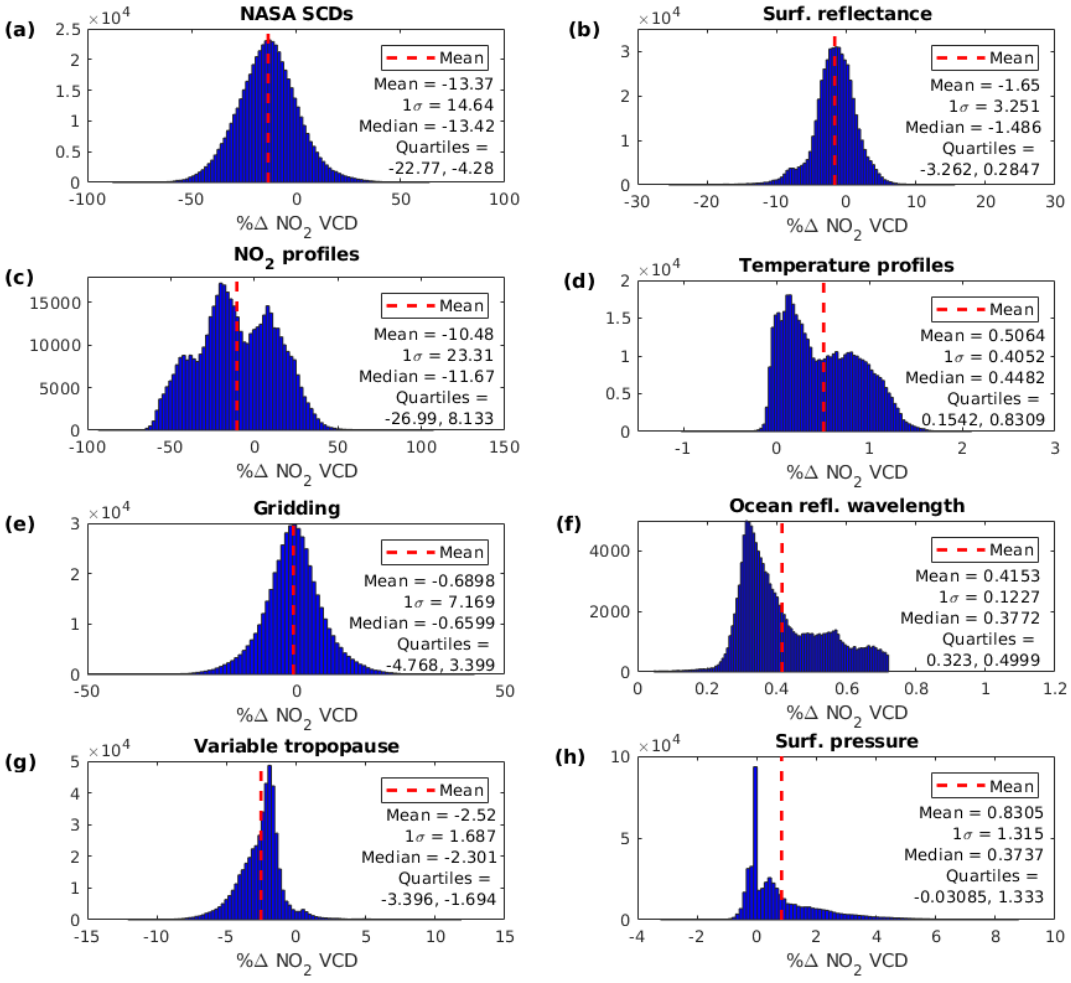

Figure S11: Histograms of the changes in JJA VCDs from Fig. 1. As in Fig. 1: **(a)** Change due to new NASA SCDs. **(b)** Change due to updated surface reflectance. **(c)** Change due to new monthly profiles. **(d)** Changes due to new temperature profile. **(e)** Changes due to new gridding method. **(f)** Changes due to the ocean reflectance changed to 460 nm. **(g)** Change due to implementation of the variable tropopause height. **(h)** Changes due to the Zhou et al. (2009) surface pressure formulation. Outliers are excluded. In **(f)**, only ocean grid cells are considered.

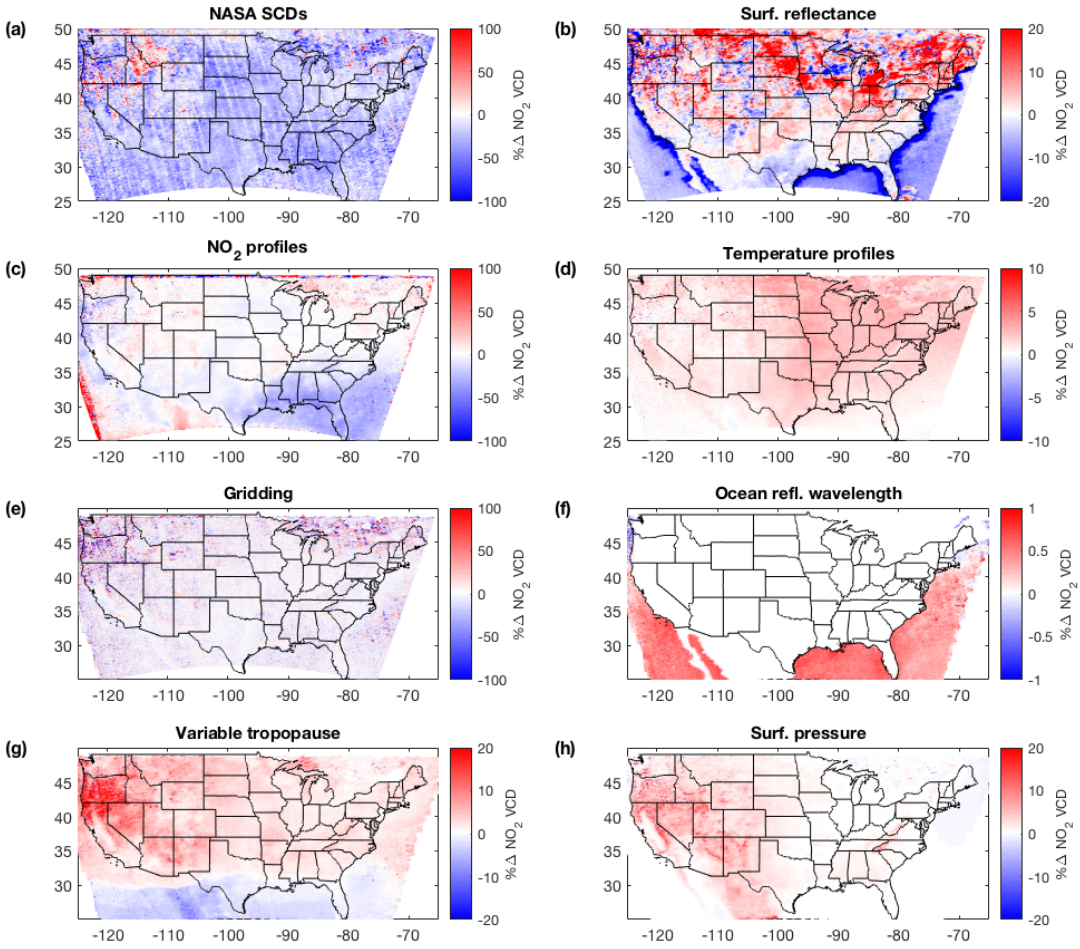

Figure S12: As Fig. 1 but for Jan, Feb, Dec 2012: changes in total tropospheric or visible-only VCDs due to individual changes. **(a)** Change due to new NASA SCDs. **(b)** Change due to updated surface reflectance. **(c)** Change due to new monthly profiles. **(d)** Changes due to new temperature profile. **(e)** Changes due to new gridding method. **(f)** Changes due to the ocean reflectance changed to 460 nm. **(g)** Change due to implementation of the variable tropopause height. **(h)** Changes due to the Zhou et al. (2009) surface pressure formulation. All averages exclude the row anomaly and use only cloud fraction ≤ 0.2.

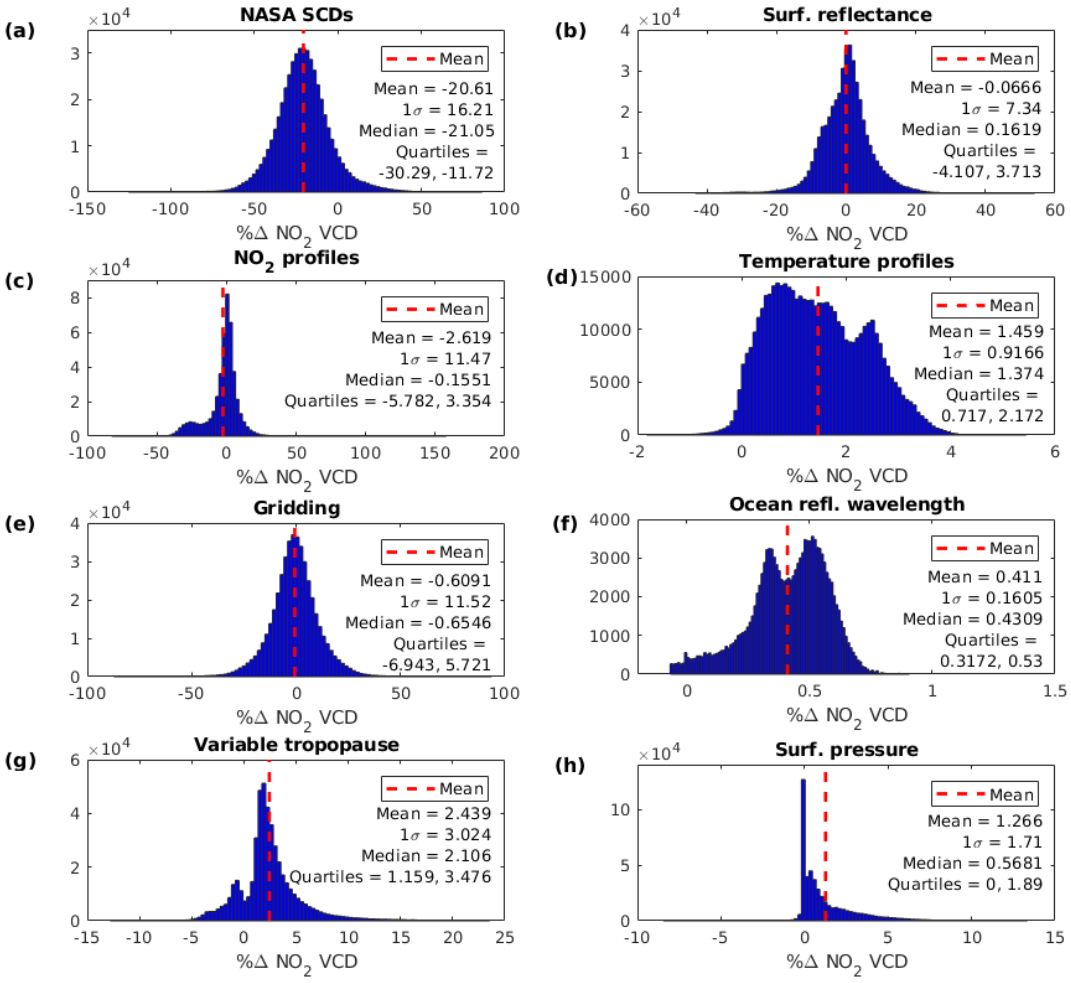

Figure S13: Histograms of the changes in DJF VCDs from Fig. S12, with outliers removed. In **(f)**, only ocean grid cells are considered.

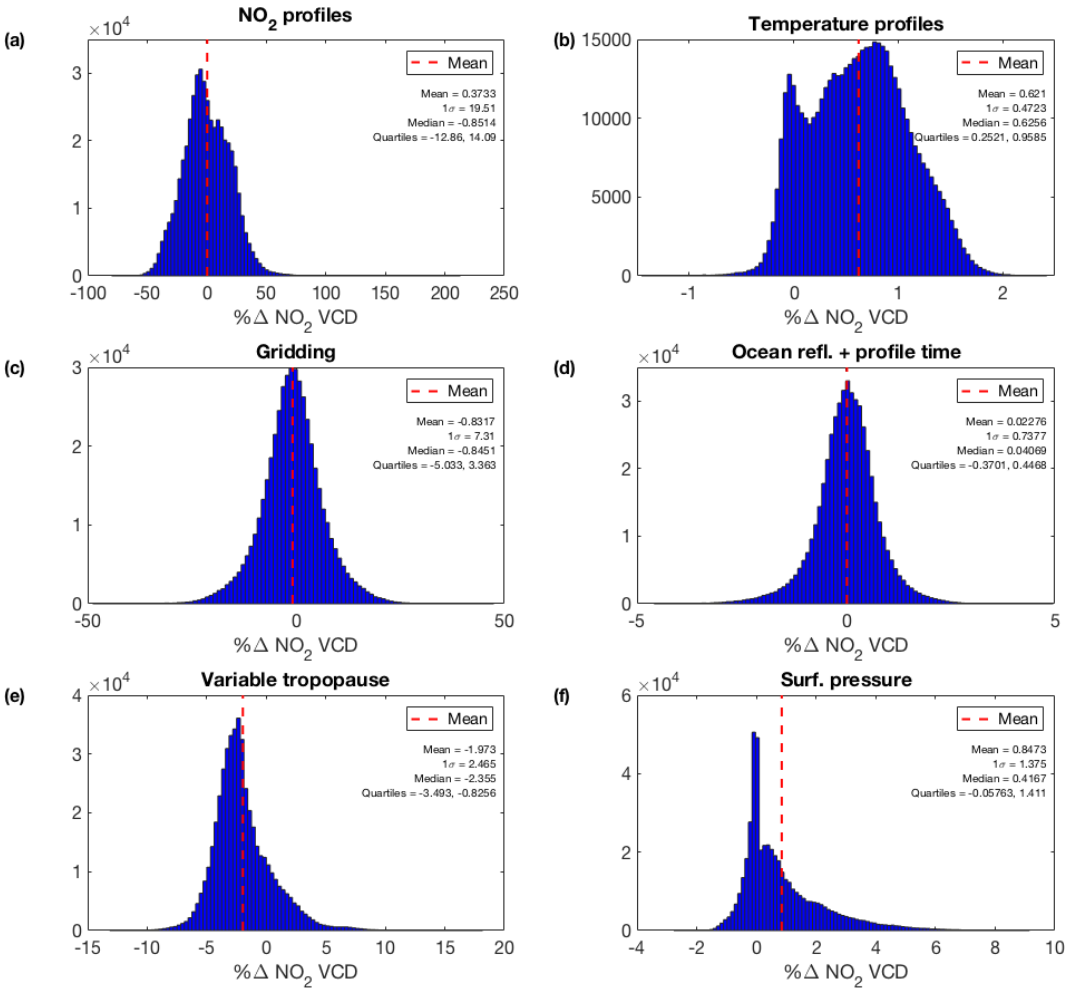

Figure S14: Histograms of the differences shown in Fig. 2 (summertime average changes in NO_2 VCDs using daily profiles). As in Fig. 2, changes due to: **(a)** implementation of new profiles, **(b)** new temperature profiles, **(c)** new gridding method, **(d)** change to temporal matching of daily profiles with OMI overpass and changing the ocean reflectance LUT to 460 nm, **(e)** implementing the variable tropopause height, and **(f)** the Zhou et al. (2009) surface pressure formulation.

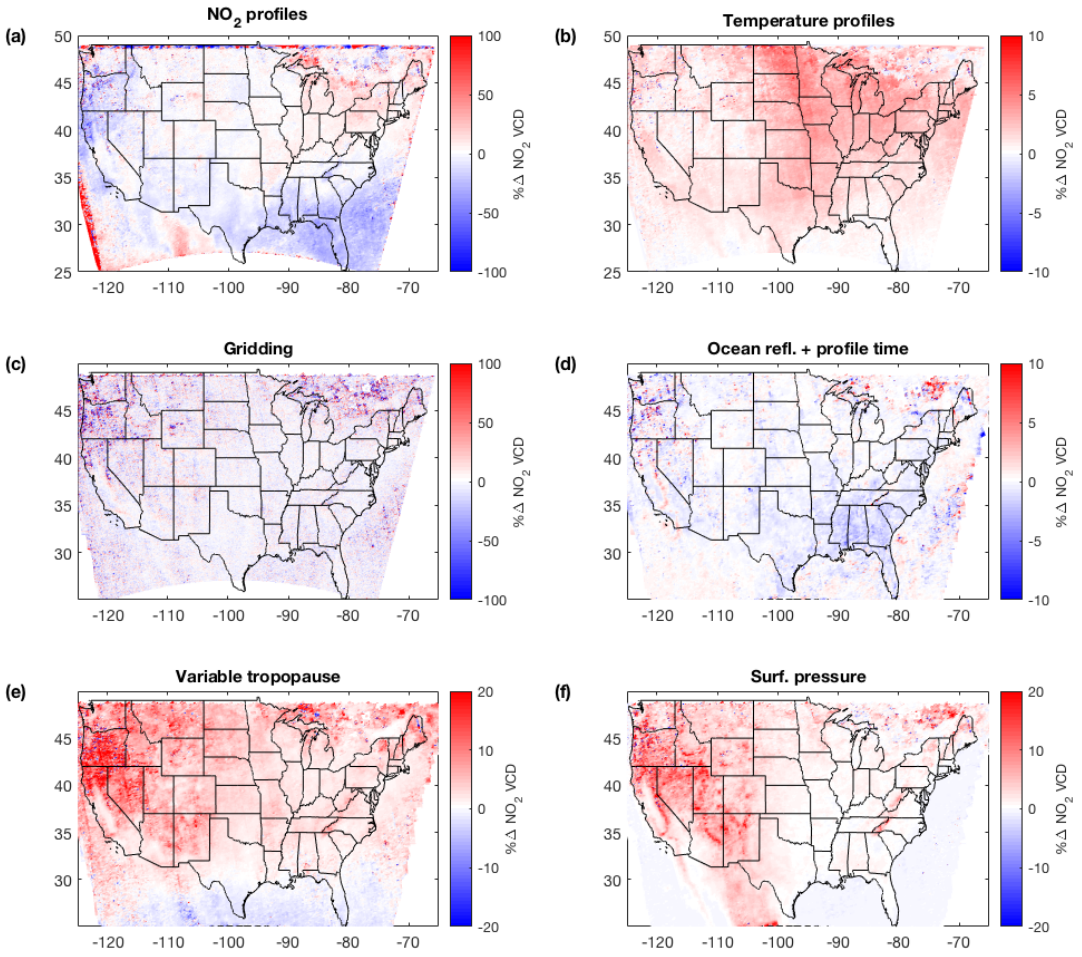

Figure S15: Similar to Fig. 2, but for DJF. Changes in the average VCDs in the subproduct using daily profiles due to: **(a)** implementation of new profiles, **(b)** new temperature profiles, **(c)** new gridding method, **(d)** change to temporal matching of daily profiles with OMI overpass and changing the ocean reflectance LUT to 460 nm, **(e)** implementing the variable tropopause height, and **(f)** the Zhou et al. (2009) surface pressure formulation. All averages exclude the row anomaly only use cloud fraction ≤ 0.2.

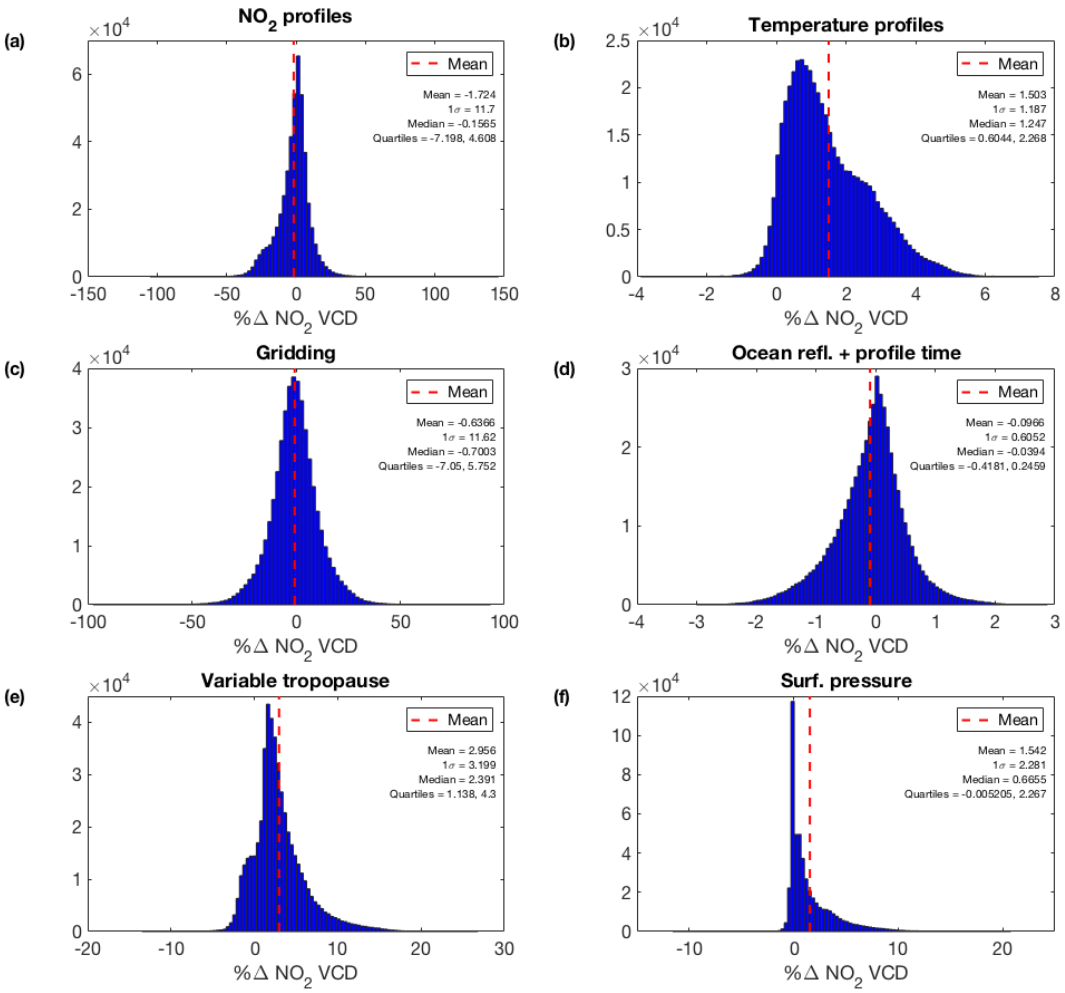

Figure S16: Histogram of the differences in Fig. S15, with outliers removed.

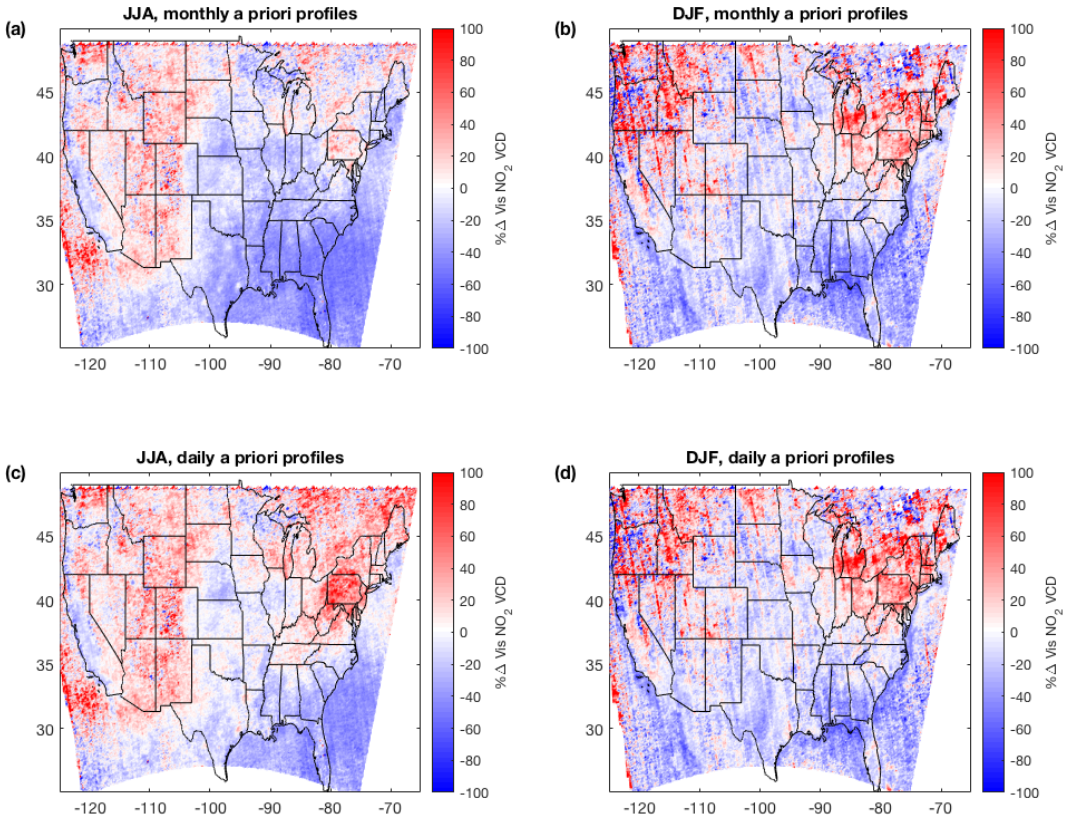

Figure S17: As Fig. 6 but for the visible-only VCDs: overall differences between v2.1C and v3.0B **(a,b)** v3.0B uses monthly profiles. **(c,d)** v3.0B uses daily profiles. **(a,c)** average over Jun–Aug 2012. **(b,d)** average over Jan, Feb, Dec 2012. All averages exclude the row anomaly and use only cloud fraction ≤ 0.2.

References

Bacak, A., Cooke, M., Bardwell, M., McGillen, M., Archibald, A., Huey, L., Tanner, D., Utembe, S., Jenkin, M., Derwent, R., Shallcross, D., and Percival, C.: Kinetics of the HO_2 + NO_2 Reaction: On the impact of new gas-phase kinetic data for the formation of HO_2NO_2 on HO_x, NO_x and HO_2NO_2 levels in the troposphere, Atmos. Environ., 45, 6414–6422, doi: 10.1016/j.atmosenv.2011.08.008, URL https://doi.org/10.1016/j.atmosenv.2011.08.008, 2011.

Brown, S. S., Dubé, W. P., Fuchs, H., Ryerson, T. B., Wollny, A. G., Brock, C. A., Bahreini, R., Middlebrook, A. M., Neuman, J. A., Atlas, E., Roberts, J. M., Osthoff, H. D., Trainer, M., Fehsenfeld, F. C., and Ravishankara, A. R.: Reactive uptake coefficients for N2O5determined from aircraft measurements during the Second Texas Air Quality Study: Comparison to current model parameterizations, J. Geophys. Res., 114, doi: 10.1029/2008jd011679, URL https://doi.org/10.1029/2008jd011679, 2009.

Cahalan, R. F., Ridgway, W., Wiscombe, W. J., Gollmer, S., and Harshvardhan: Independent Pixel and Monte Carlo Estimates of Stratocumulus Albedo, J. Atmos. Sci., 51, 3776–3790, doi: 10.1175/1520-0469(1994)051⟨3776:ipamce⟩2.0.co;2, URL https://doi.org/10.1175/1520-0469(1994)051<3776:ipamce>2.0.co;2, 1994.

Evans, M. J. and Jacob, D. J.: Impact of new laboratory studies of N2O5hydrolysis on global model budgets of tropospheric nitrogen oxides, ozone, and OH, Geophys. Res. Lett., 32, doi: 10.1029/2005gl022469, URL https://doi.org/10.1029/2005gl022469, 2005.

Henderson, B. H., Pinder, R. W., Crooks, J., Cohen, R. C., Carlton, A. G., Pye, H. O. T., and Vizuete, W.: Combining Bayesian methods and aircraft observations to constrain the $HO^{\cdot}$ + NO_2 reaction rate, Atmospheric Chemistry and Physics, 12, 653–667, doi: 10.5194/acp-12-653-2012, URL https://www.atmos-chem-phys.net/12/653/2012/, 2012.

Laughner, J. L., Zare, A., and Cohen, R. C.: Effects of daily meteorology on the interpretation of space-based remote sensing of NO_2, Atmos. Chem. Phys., 16, 15 247–15 264, doi: 10.5194/acp-16-15247-2016, URL http://www.atmos-chem-phys.net/16/15247/2016/, 2016.

Marshak, A., Davis, A., Cahalan, R., and Wiscombe, W.: Nonlocal independent pixel approximation: direct and inverse problems, IEEE Trans. Geosci. Rem. Sens., 36, 192–205, doi: 10.1109/36.655329, URL https://doi.org/10.1109/36.655329, 1998.

Nault, B. A., Laughner, J. L., Wooldridge, P. J., Crounse, J. D., Dibb, J., Diskin, G., Peischl, J., Podolske, J. R., Pollack, I. B., Ryerson, T. B., Scheuer, E., Wennberg, P. O., and Cohen, R. C.: Lightning NO_x Emissions: Reconciling Measured and Modeled Estimates With Updated NO_x Chemistry, Geophys. Res. Lett., doi: 10.1002/2017GL074436, 2017.

Sander, S. P., Friedl, R. R., Abbatt, J. P. D., Barker, J. R., Burkholder, J. B., Golden, D. M., Kolb, C. E., Kurylo, M. J., Moortgat, G. K., Wine, P. H., Huie, R. E., and Orkin, V. L.: Chemical Kinetics and Photochemical Data for Use in Atmospheric Studies: Evaluation Number 17, Tech. rep., Jet Propulsion Laboratory, 2011.

Zhou, Y., Brunner, D., Boersma, K. F., Dirksen, R., and Wang, P.: An improved tropospheric NO_2 retrieval for OMI observations in the vicinity of mountainous terrain, Atmos. Meas. Tech., 2, 401–416, doi: 10.5194/amt-2-401-2009, URL https://www.atmos-meas-tech.net/2/401/2009/, 2009.